Crystal structures and formation mechanisms of boron-rich tungsten borides

Chao Gu,[1] Yongcheng Liang,[2,*] Xuefeng Zhou,[1] Jian Chen,[1] Dejiang Ma,[1] Jiaqian Qin,[3] Wenqing Zhang,[1] Qiang Zhang,[4] Luke L. Daemen,[4] Yusheng Zhao,[1] and Shanmin Wang[1,†]

[1]*Department of Physics and Academy for Advanced Interdisciplinary Studies, Southern University of Science and Technology, Shenzhen 518055, China*

[2]*College of Science, Institute of Functional Materials, and State Key Laboratory for Modification of Chemical Fibers and Polymer Materials, Donghua University, Shanghai 201620, China*

[3]*Metallurgy and Materials Science Research Institute, Chulalongkorn University, Bangkok 10330, Thailand*

[4]*Neutron Science Division, Oak Ridge National Laboratory, Oak Ridge, Tennessee 37831, USA*

(Received 10 June 2021; revised 9 July 2021; accepted 9 July 2021; published 22 July 2021)

Boron-rich tungsten borides tend to adopt mechanically unfavorable layered structures but experimentally exhibit excellent mechanical properties rivalling traditional superhard solids. Unravelling the contraindicated structure-property relationship, however, has been impeded by their structural ambiguities because of the difficulty in probing boron and atomic deficiency of these borides. Here, we study crystal structures of boron-rich tungsten borides WB_{3+x} and WB_{2+x} by neutron diffraction based on high-quality samples prepared by a high-pressure method, leading to definitive structural resolutions for both borides with unique compositions of $WB_{5.14}$ and $WB_{2.34}$. Combined with theoretical calculations, their structural stability is revealed to be closely related to atomic deficiency, which is governed by the valence-band filling with an optimal valence-electron concentration of ~10 per cell. The presence of interstitial boron trimers at the vacant W : 2*b* sites in $WB_{5.14}$ alters the crystal symmetry, making the Wyckoff 2*d* site more favorably occupied by W, rather than the 2*c* site, as previously misassigned. The staggered planar boron layers and wrinkled boron bonding in $WB_{2.34}$ are identified to be crucial for stabilizing its structure. These findings unveil the longstanding structural mysteries of boron-rich tungsten borides and offer powerful insights for rational design of borides by defect chemistry.

DOI: 10.1103/PhysRevB.104.014110

I. INTRODUCTION

Boron with one electron less than carbon favors forming a triangular B3 motif (i.e., trimer unit) with three-center bonds that can assemble into various polyhedral boron bonding networks in boron-rich solids (e.g., B_6O) [1,2]. The situation is greatly changed for metal borides because the metal can donate electrons, making the electron-deficient boron more like carbon [3], resulting in graphenelike boron nets for most metal diborides with the AlB_2-type structure [Fig. 1(a)] [4]. However, for transition-metal (TM) diborides, such a structure becomes unstable with increasing valence electrons, leading to the formation of exotic borides. Of particular interest are boron-rich tungsten borides of WB_{3+x} (or WB_4) and WB_{2+x} (or W_2B_5) with superior mechanical properties rivalling those of traditional superhard solids [5–19], making them promising for practical applications as machining tools with significantly promoted efficiency over traditional carbides and superhard materials. However, their crystal structures and compositions have remained elusive for over half a century [13,20–22], impeding understanding of their property-structure relationships.

The challenge for accurately determining their structures is mainly related to boron that is electron poor and nearly transparent to both x rays and electron diffractions, in stark contrast to TM atoms that eventually dominate the overall structural factor. Although, based on x-ray diffraction (XRD) measurement, the same $P6_3/mmc$ symmetry was assigned for both WB_{3+x} and WB_{2+x} with different atomic positions and vacancies [13,20,21,23], their definitive crystal structures and compositions are still under debate. For WB_{3+x}, WB_4 was initially proposed by occupying the Wyckoff 2*d* site with exotic B2 dimers to accommodate the experimentally determined stoichiometry [Fig. 1(b)] [21]. However, recent calculations showed that such interstitial dimers destabilize its structure [24–29], leading to a dimer-free model of WB_3 [Fig. 1(c)] [25–30]. Although WB_3 is thermodynamically stable, its structure involves a profound softening under indentation as predicted with a relatively low hardness [31], in contradiction to experiments. Additionally, a few other structural models with different interstitial boron and atomic deficiencies were also proposed [13,23,32–34], but they all were quickly invalidated [18,35]. Regarding WB_{2+x}, its structure and composition are also contentious issues; conflicting reports include $hP3$-WB_2 [Fig. 1(a)] [36], two distinct $hP12$-WB_2 structures with differently occupied Wyckoff 2*c* or 2*d* site by boron [Figs. 1(e) and 1(f)] [37,38], $hP14$-W_2B_5 [Fig. 1(g)] [20,21], and other predicted structures [28,39]. A throughout overview of WB_{3+x} and WB_{2+x} can be found in Ref. [13]. Clearly, structural ambiguities of both borides cannot be clarified based on conventional x-ray-only experiments.

The neutron diffraction is in this regard the best probe for determining boron (i.e., isotope ^{11}B) with a neutron scatting

*ycliang@dhu.edu.cn
†wangsm@sustech.edu.cn

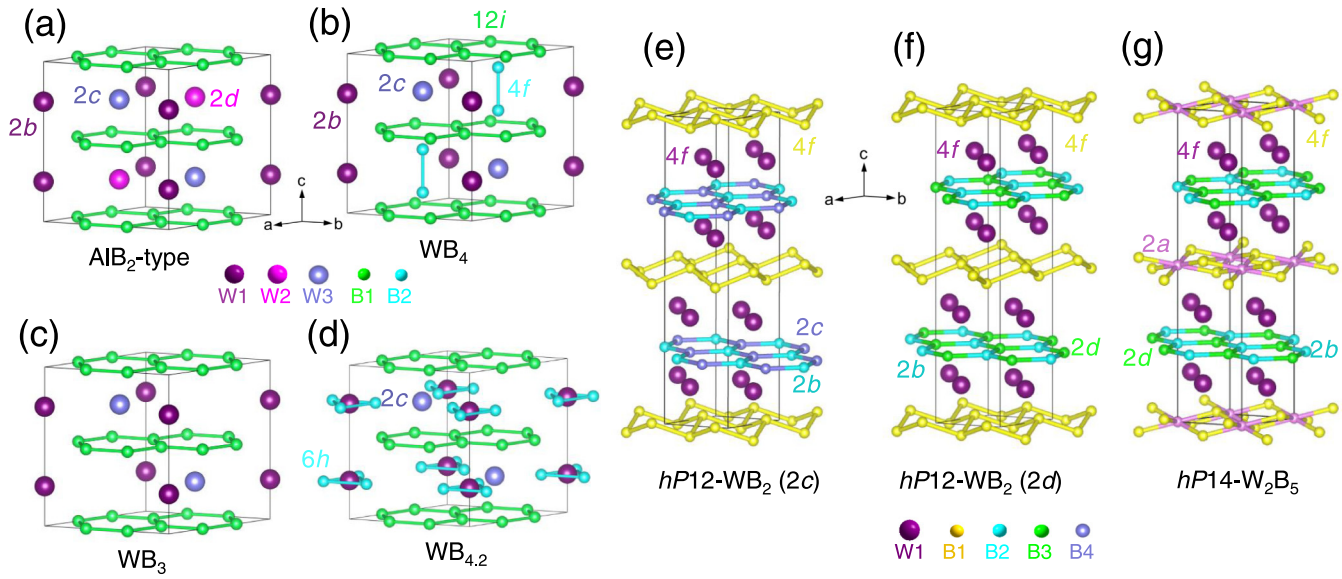

FIG. 1. Possible structures for WB_{3+x} and WB_{2+x} with various compositions. (a) AlB_2-type WB_2 (i.e., *hP*3). The symmetry of the AlB_2-type structure is *P*6/*mmm* (No. 191), which can be equivalently described by $P6_3/mmc$ (No. 194) with appropriately constrained atomic positions. (b)–(d) Possible structures of WB_{3+x}: WB_4 (Ref. [20]), WB_3 (Ref. [25]), and $WB_{4.2}$ (Ref. [34]). (e)–(g) Possible structures of WB_{2+x}: (e) *hP*12-WB_2 (2*c*) with occupied Wyckoff 2*c* site by boron (Ref. [37]), (f) *hP*12-WB_2 (2*d*) with occupied Wyckoff 2*d* site by boron (Ref. [36]), and (g) *hP*14-W_2B_5 (i.e., *hP*14-$WB_{2.5}$) (Refs. [27,38]). Structures in (b)–(g) have the same symmetry of $P6_3/mmc$.

length even greater than that of W [40], but it suffers from difficulties in preparing a high-quality ^{11}B-enriched sample by traditional methods because excess boron is often involved in the final products and largely exacerbates structural refinements [35]. Recently, a composition of $WB_{4.2}$ was determined for WB_{3+x} by Lech *et al.* [35], using neutron powder diffraction (NPD) measurements based on a sample with heavy boron impurity. A prominent feature of $WB_{4.2}$ is the randomly distributed interstitial B3 trimers at metal-deficient sites [Fig. 1(d)]. This structure was also lent support from calculations using ordered orthorhombic models of *Cmcm*-$WB_{4.2}$ [41] and *Pmmn*-WB_{5-x} [42] as structural approximates to relax the stringent requirement for computing sources; both orthorhombic phases have the same average global symmetry of $P6_3/mmc$ to that of WB_{3+x} [41–45]. Although the Wyckoff 2*c* and 2*d* sites in WB_3 are equivalent, they become distinguishable in $WB_{4.2}$ because the B3 trimers have certain crystallographic orientation and alter the crystal symmetry, calling into question the adequacy of the $WB_{4.2}$ model.

With these aims, here, we formulate a high-pressure (*P*) route for synthesis of high-quality WB_{3+x} and WB_{2+x} samples without boron impurity for NPD experiments, leading to a definitive resolution of their structures. Mysteries of their phase stability and formation mechanism are revealed to link to an optimal filling of valence states. This paper advances our understanding of the crucial role of atomic vacancies played in TM borides, which would stimulate more research efforts for discovering borides by tailoring vacancies.

II. EXPERIMENT DETAILS

A. Sample synthesis

$W^{11}B_{3+x}$ and $W^{11}B_{2+x}$ samples were prepared from the reactions between WCl_6 (99.6%) and $Na^{11}BH_4$ (99.5%) in the same molar ratio of 1:12 at 5 GPa and different temperatures (*T*) of 2300 and 1800 °C, respectively. Excess $Na^{11}BH_4$ was used to establish a boron-rich environment for producing high borides of tungsten. High-*P* syntheses were carried out in a DS 6 × 10 NM cubic press installed at the high-*P* lab of SUSTech with a largely extended temperature capability up to 3700 °C using our cell assembly [46], which is very suitable for synthesis of refractory materials. Before the experiment, the starting materials were homogenously mixed and compressed into a pellet, which was then loaded in a *h*BN capsule and assembled with the preprepared cell parts for high-*P* synthesis. Due to the sensitivity of chloride precursor to air, all procedures were done in a glove box with an Ar atmosphere. Both WB_{3+x} and WB_{2+x} can coexist in a wide temperature range of 2200–2900 °C at 5 GPa, and the addition of NaCl can largely suppress the formation of WB_{2+x}. More experimental details can be found elsewhere [46]. The recovered samples were readily purified by washing with water to remove unreacted precursors and other byproducts. For comparison, WB_{3+x} and WB_{2+x} samples were also synthesized by direct reactions of homogenously mixed W (∼3 μm, 99.9%) and B (∼15 μm, 99.9%) powders in molar ratios of 1:2.5 and 1:10, respectively, under the similar high-*P*-*T* conditions of 5 GPa and 1800–2600 °C. To alleviate the layer stacking faults in WB_{2+x}, it was also prepared by the reaction between WO_3 and $NaBH_4$ with a molar ratio of 1:24 at 5 GPa and 2200 °C.

B. Sample characterization

The recovered samples were checked by an x-ray diffractometer equipped with a copper target at room temperature. Neutron diffraction measurements were conducted at the POWGEN beamline of SNS/ORNL. Structural refinements were performed using the GSAS program [47]. The sample

morphologies and microstructures were observed by scanning electron microscopy (SEM) and transmission electron microscopy (TEM). More experimental descriptions are given in the Supplemental Material [48].

C. Calculations

The calculations were carried out using density functional theory within the framework of Vienna *ab initio* Simulation Package (VASP) [49], which employs a plane-wave basis with a projector augmented wave [50]. The generalized gradient approximation with Perdew-Burke-Ernzerhof function was adopted as electron exchange-correlation interactions [51]. A large cutoff energy of 500 eV and dense k meshes were chosen to ensure that the total-energy calculations were converged to within 1 meV/atom. Forces on the ions were calculated through the Hellmann-Feynman theorem, allowing a full geometry optimization of structures. The formation energies (ΔE) of the involved metal borides were evaluated based on the relaxed structures, according to $\Delta E(\mathrm{TMB}_x) = E(\mathrm{TMB}_x) - E(\mathrm{TM}) - xE(\mathrm{B})$, where $E(\mathrm{TMB}_x)$, $E(\mathrm{TM})$, and $E(\mathrm{B})$ denote the total energies of TMB_x, TM, and α-B, respectively.

III. RESULTS AND DISCUSSION

A major disadvantage of the traditional methods for synthesizing boron-rich TM borides often involves super-excess boron in the recovered samples, as reported for $WB_{4.2}$ and $Mo_{0.757}B_3$ with starting TM:B ratios of 1:12 and 1:6, respectively, using arc melting and high-P methods [35,52]. Although the presence of excess boron is necessary for the suppression of other TM boride byproducts, it can hardly be separated from the final sample and produces complex and strong NPD peaks that largely overlap with those of the target material. Additionally, such excess boron contributes weak XRD peaks at high d spacing, which would lead to misassignment of the symmetry of boride, as occurred in WB_4 with an initially misassigned tetragonal structure [53]. Thus, accurately determining crystal structures of boron-rich TM borides is still challenging, and many existing reports appear to be in contradiction. To settle this issue, we prepared boron-free WB_x using WCl_6 and $NaBH_4$ as starting reactants, given by

$$\mathrm{WCl_6} + x\mathrm{NaBH_4} = \mathrm{WB}_x + x\mathrm{NaCl} + (6-x)\mathrm{HCl} + \frac{5x-6}{2}\mathrm{H_2}, \quad (1)$$

where the byproduct NaCl was identified by XRD measurement, and a sharp smell of acid released from the recovered sample suggests the presence of HCl gas. Similar reactions have been successfully used for synthesis of several TM diborides at ambient pressure [54–56]. Apparently, both precursors contain the highest and lowest oxidation states of W^{6+} cations and B^{5-} anions, and they are energetically more favorable for forming boron-rich borides, especially under pressure, which can effectively prompt more d electrons of TM to participate in the chemical bonding with boron.

To obtain boron-rich borides, super-excess $NaBH_4$ was added with a molar ratio of $WCl_6 : NaBH_4 = 1 : 12$. A prominent advantage of this method is that all the involved byproducts and unreacted precursors are soluble in water, which facilitates sample purification, in striking contrast to the traditional methods. As expected, the final products were high-quality boron-rich borides without involving unwanted boron (Fig. 2). For the sample synthesized at 5 GPa and 2300 °C [Fig. 2(a)], the recovered product was a highly dense polycrystalline bulk sample instead of well-dispersed powders, implying that it may form from a melting process [Fig. 2(b)]. Most of the strong XRD reflection lines in Fig. 2(a) can be well indexed by either WB_3, WB_4, or $WB_{4.2}$, as they appear consistent with XRD data alone, while the remaining weak peaks can match those of the reported $hP12$-WB_2 and $hP14$-W_2B_5. We find that both phases can coexist in a wide temperature range of 2200–2900 °C at 5 GPa.

As the synthesis temperature decreases, WB_{2+x} is thermodynamically more favored, and its single phase can be readily obtained at 5 GPa and 1800 °C [Fig. 2(c)], displaying uniformly distributed submicron grains [Fig. 2(d)]. However, the XRD peak profile of this sample is unusual, and the 10l lines are anomalously broadened (e.g., 103, 104, and 105) (Fig. S1 in the Supplemental Material [48]), due to the layer stacking disorder, as frequently reported in layer-structured systems [57–59]. Clear Moiré fringes are observed by TEM in Fig. 2(e), which confirms such layer stacking disorder with an interlayer rotation angle of 13.6° [60] (Fig. S2 in the Supplemental Material [48]) and explains the peak intensity mismatch between the simulated and observed XRD [Fig. 2(c)]. In fact, a similar phenomenon is also observed in the samples synthesized from the reaction between W and B at 5 GPa and 1800 °C (Fig. S3 in the Supplemental Material [48]). The situation can be profoundly improved for the samples synthesized at extremely high temperature of 3000 °C or using WO_3 and $NaBH_4$ as precursors (Figs. S3 and S4 in the Supplemental Material [48]). Importantly, the final borides are boron free, which is beneficial to obtain high-quality NPD data.

To accurately determine the crystal structures and compositions of both borides, we performed NPD measurements on high-P synthesized samples (Fig. 3), and the observed NPD profiles are significantly different from those of their XRD patterns (Fig. 2). For WB_{3+x}, a series of new and strong NPD peaks emerge including 021, 030, 032, and 034 [Fig. 3(a)], concurrent with the absence of the 101 peak. The situation in WB_{2+x} is much more remarkable, and its NPD pattern displays a set of almost completely different lines such as 010, 012, 013, 015, and 016 (i.e., 0hk). Clearly, these 0hk peaks only appear in the NPD pattern and should be closely associated with the boron sublattice, due to the sensitivity of ^{11}B to neutron scattering with a coherent scattering length (i.e., 6.65) ~37% larger than that of W (i.e., 4.86) [40]. Thus, the overall neutron scattering powers of these borides are dominated by both B and W atoms, allowing us to reliably extract their structure parameters.

Using the WB_3 model as an initial attempt, all the NPD reflection lines of WB_{3+x} in Fig. 3(a) can be indexed (Fig. S5 in the Supplemental Material [48]), but with obvious discrepancies in peak intensity (e.g., 110, 021, and 032 lines), indicating the WB_3 model is not adequate. Such structural

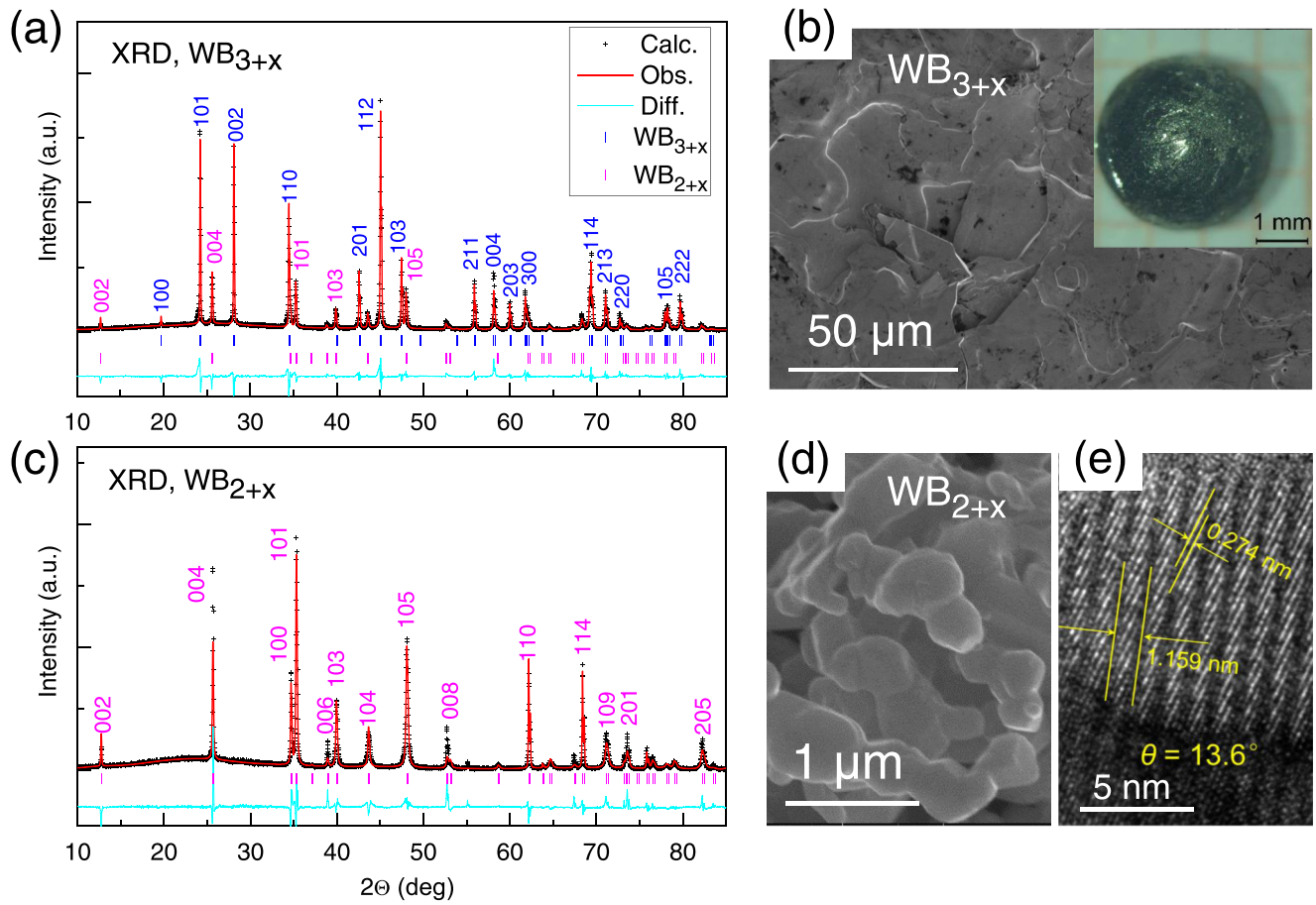

FIG. 2. X-ray diffraction (XRD) and scanning electron microscopy (SEM) measurements of WB_{3+x} and WB_{2+x}. (a) Refined XRD pattern for WB_{3+x} with WB_{2+x} as the only byproduct. (b) SEM image of WB_{3+x}. Inset is an optical image of bulk WB_{3+x}. (c) Refined XRD pattern for WB_{2+x}. (d) SEM image of WB_{2+x}. (e) transmission electron microscopy (TEM) observation of Moiré fringe because of layer stacking disorder with a layer rotation angle of ∼13.6° (Fig. S2 in the Supplemental Material [48]).

inadequacy is also demonstrated in the XRD pattern with a largely enhanced intensity of the 100 peak (Fig. S5 in the Supplemental Material [48]), inconsistent with observations. In fact, the best refinement based on the WB_3 model leads to a composition of $WB_{4.5}$ with partially occupied W sites; however, the observed peak intensity still cannot be appropriately reproduced using such refined $WB_{4.5}$ (Fig. S6 in the Supplemental Material [48]). Note that Wyckoff 2*c* and 2*d* sites in WB_3 are equivalent for locating W atoms, producing the same XRD and NPD patterns (Fig. S5 in the Supplemental Material [48]).

We thus attempted to refine the structure of WB_{3+x} using the $WB_{4.2}$ model with B3 trimers [Figs. 1(d) and 4(a)]. However, it is worthwhile to mention that the occupation of the Wyckoff 6*h* site with B3 trimer units lowers the symmetry of $P6_3/mmc$, which makes both 2*c* and 2*d* sites no longer equivalent for being occupied by W atoms. Obviously, for the case of occupying 2*c* sites with W atoms, three vertices of the B3 trimer point to three W : 2*c* atoms [Fig. 4(a)], in contrast to that of the W : 2*d* structural model with three vertices pointing to voids [Fig. 4(b)]. The former results in the absence and presence of 021 and 121 peaks [Fig. 4(c)], respectively, suggesting there may exist misassigned atomic positions in the $WB_{4.2}$ model, as recently proposed by Lech *et al.* [35]. The misassignment is likely related to W : 2*c* positions because the B3 trimers in $WB_{4.2}$ have a specific crystallographic orientation. For both structural models, the XRD patterns are also calculated and plotted in Fig. 4(d). The replacement of the 2*d* site with the 2*c* site leads to a strong 100 peak, which is inconsistent with observations. Clearly, the Wyckoff 2*d* is more appropriate for accommodating W atoms, rather than the 2*c* site, although both models can produce nearly the same composition of $WB_{5.14}$. Accordingly, we replaced the Wyckoff 2*c* site with 2*d* in $WB_{4.2}$ and applied this modified model for WB_{3+x}, achieving an excellently refined NPD pattern [Figs. 3(a) and Fig. S7 in the Supplemental Material [48]). The refined lattice parameters at 300 K are summarized in Table I, and the crystal structures are depicted in Figs. 3(b)–3(d).

The thus-refined composition of WB_{3+x} is $WB_{5.14}$ with refined boron positions like those reported in Ref. [35]. Compared with B : 12*i* sites that are highly occupied for forming the flat boron net, all other sites involve fractional occupations including W : 2*b*, W : 2*d*, and B : 6*h* (Table I). The triangular B3 motif is made of B : 6*h* atoms with the center of mass located at the vacant W : 2*b* [Figs. 3(b)–3(d)], signifying an electron-deficient local environment surrounding these sites. This also suggests that both the W : 2*b* and B3 trimer cannot

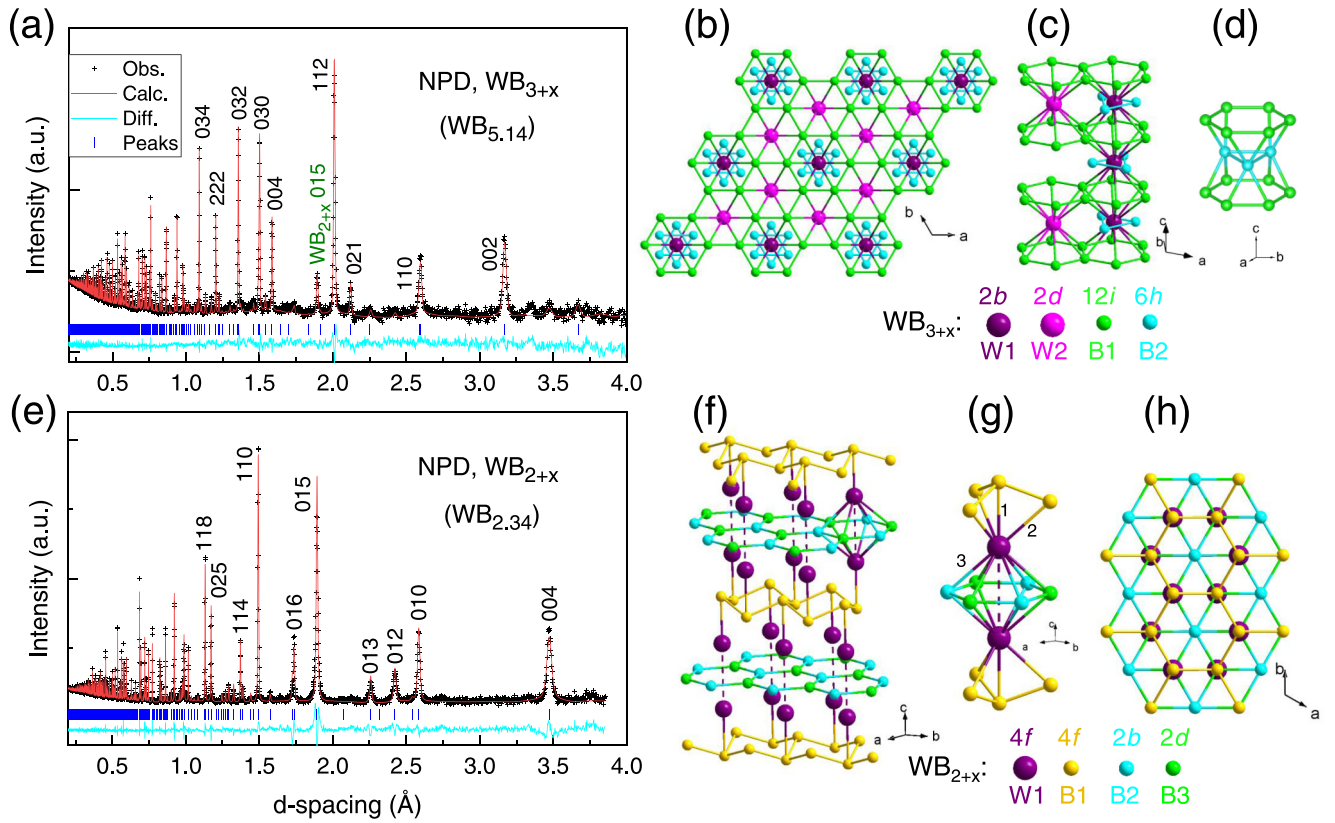

FIG. 3. Structural refinements for WB_{3+x} and WB_{2+x} based on neutron diffraction data taken at ambient conditions. (a)–(c) Refined neutron powder diffraction (NPD) pattern for WB_{3+x} and its crystal structures. (d)–(g) Refined NPD pattern for WB_{2+x} and its crystal structures. Shown in (c) and (f) are their characteristic structural units. The W-B bonds numbered with 1, 2, and 3 have lengths of 2.235, 2.341, and 2.327 Å, respectively. Both samples used in the NPD measurements are the same as those in XRD experiments (Fig. 2).

coexist at the same site because the presence of metal donates excess electrons to boron and destabilizes the trimer unit. In addition, the determined edge length of the trimer is only 1.858 Å with a limited interstitial space for accommodating a big W atom. Note that the refined occupancy of the B3 trimer is only 0.3735, smaller than that of W : 2*b* vacancies (i.e., 0.441), indicating that there exist ~6% voids at 2*b* sites without being occupied by either W or B3 trimer. Vacancy also occurs at W : 2*d* with an occupancy of 0.8266. Apparently, these defective features are different from previous reports [35,42] and provide insights into its crystal and electronic structures.

Despite a simple symmetry with a small unit cell, $WB_{5.14}$ contains many atoms, vacancies, and intricate multiatomic, which result in such intriguing composition and crystal structure made of the (WB_{12}) dumbbell building unit [Figs. 3(b) and 3(c)]. The partial replacement of W : 2*b* with the B3 trimer leads to a unique B15 tetradecagon unit that is randomly distributed in $WB_{5.14}$ according to our refinement [Fig. 3(d)], although nonrandom W vacancies were reported in WB_{3+x} [43] and MoB_{3+x} [52]. A couple of recent theoretical studies use orthorhombic symmetries of *Cmcm* (No. 63) and *Pmmn* (No. 59) to construct pseudohexagonal structures for indirectly modelling $WB_{4.2}$-type WB_{3+x} with ordered B3 trimers. Indeed, these models can help relax stringent requirements of computing resources, allowing evaluation of its phase stability and properties by calculations. The major difference between both models is the concentration of ordered B3 trimers, and our results show that *Cmcm*-$WB_{4.2}$ is a much better model for reproducing both the observed XRD and NPD (Figs. S8 and S9 in the Supplemental Material [48]).

For WB_{2+x}, structural models of *hP*3 [61] and *hP*6 can be immediately excluded based on XRD measurements (Fig. S10 in the Supplemental Material [48]), due to large mismatches between the simulated and observed XRD peaks. The models of *hP*12-WB_2 (2*c*), *hP*12-WB_2 (2*d*), and *hP*14-W_2B_5 produce a nearly identical XRD pattern with the observed, making them indistinguishable by the x-ray-only experiment (Fig. S10 in the Supplemental Material [48]). In contrast, our NPD simulations show that *hP*12-WB_2 (2*d*) (i.e., with B occupying the 2*d* site rather than 2*c*) is the only suitable structure for excellently reproducing the observed NPD (Fig. S11 in the Supplemental Material [48]). Using this model, we performed structural refinement for WB_{2+x}, leading to a well-refined NPD pattern in Fig. 3(e) with slight peak intensity mismatches (e.g., 004 and 015) due to the already identified layer stacking faults (Fig. 2). The refined composition for WB_{2+x} is $WB_{2.34}$, close to the previously reported stoichiometry of $WB_{2.27}$ as measured by both the wet chemical analysis and x-ray microprobe [21]. The obtained lattice parameters are listed in Table I, and its crystal structures are illustrated in Figs. 3(f)–3(h).

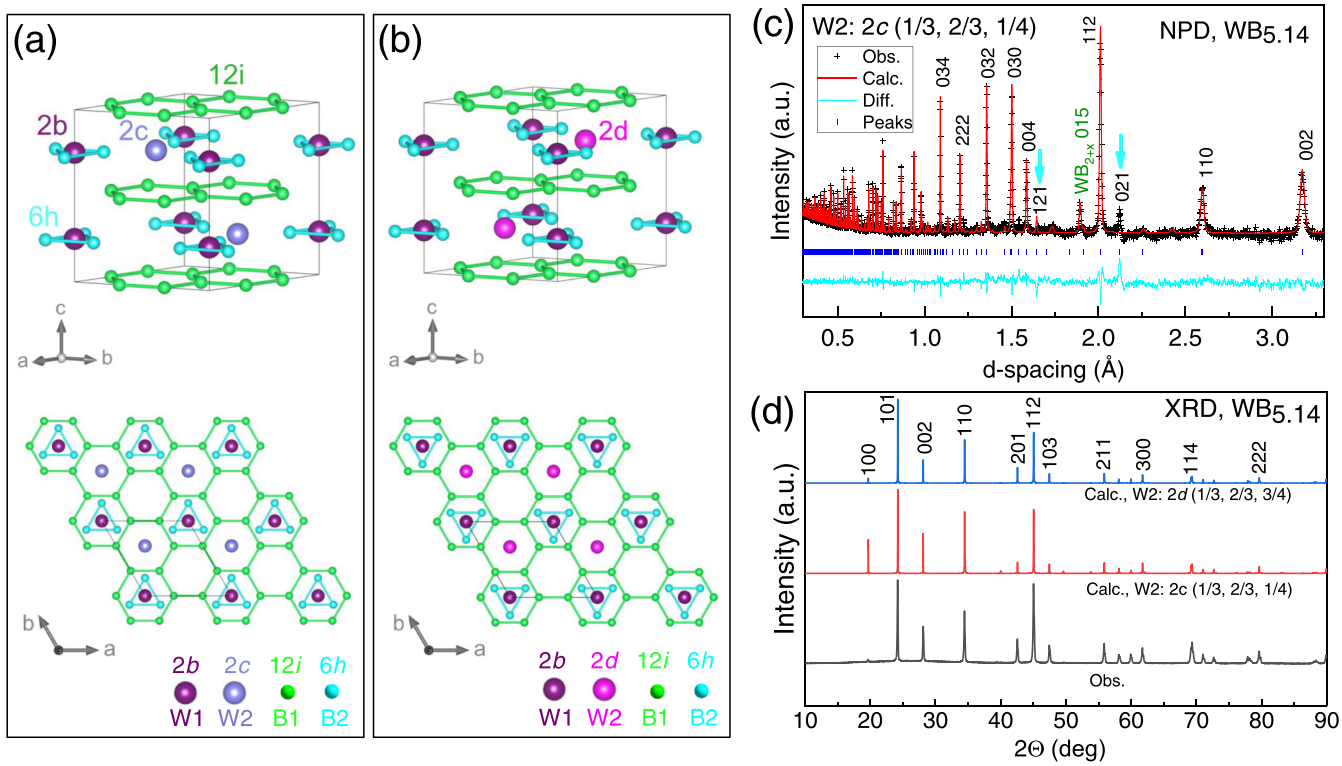

FIG. 4. Wyckoff $2c(\frac{1}{3}, \frac{2}{3}, \frac{1}{4})$ vs $2d(\frac{1}{3}, \frac{2}{3}, \frac{3}{4})$ for W in WB_{3+x} (i.e., $WB_{5.14}$). (a) and (b) Crystal structures of $WB_{5.14}$ with occupied $2c$ and $2d$ for W2 atoms, respectively. The bottom panel of each figure shows a different view of the crystal structure along the c axis. (c) Refined neutron powder diffraction (NPD) patterns for structural models in (a). (d) Calculated x-ray diffraction (XRD) patterns for $WB_{5.14}$ with two different W2 positions. In (c) and (d), Wyckoff sites for W1, B1, and B2 atoms remain invariant during calculations and refinements (see Table I).

The metal interlayers of $WB_{2.34}$ are separated and sandwiched by alternated flat and wrinkled boron sheets [Fig. 3(f)]; thus, $hP12$-WB_{2+x} is an intermediate between AlB_2- and ReB_2-type phases (Fig. S10 in the Supplemental Material [48]). Puckering of the flat B sheets is probably induced by excess electrons as denoted by metal [4]. A relative in-plane shift of the wrinkled boron sheets causes overlap of the associated B and W atoms along the c axis [Figs. 3(f)–3(h)], resulting in three different W-B bond lengths of 2.235, 2.341, and 2.327 Å, slightly shorter than that of 2.348 Å in $WB_{5.14}$. The shortest bond (i.e., 2.235 Å) is formed between W and B of the adjacent wrinkled sheet along the c axis through a strong hybridization of W : $5d_z{}^2$ and B : p_z orbitals, which is crucial for stabilizing the $hP12$ structure.

Like $WB_{5.14}$, $WB_{2.34}$ also has complicated fractional atomic occupations (Table I). The obtained vacancy fractions in the W-W layer and wrinkled B sheet are ∼26 and 8%, respectively. Contrary to what one might expect, both B : $2b$

TABLE I. Summary of refined lattice parameters for WB_{3+x} and WB_{2+x} based on NPD data taken at 300 K (see Fig. 3).

	WB_{3+x} (300 K)		WB_{2+x} (300 K)	
Formula	$WB_{5.14}$		$WB_{2.34}$	
System	$P6_3/mmc$ (No. 194)		$P6_3/mmc$ (No. 194)	
a, c (Å)	$a = 5.2001(1)$, $c = 6.3443(1)$		$a = 2.9853(2)$, $c = 13.8915(2)$	
Volume (Å^3)	148.5720		107.2130	
Density (g/cm^3)	7.4150		9.3126	
	Site	Occupancy	Site	Occupancy
Atomic positions	W1 : $2b(0, 0, \frac{1}{4})$	0.5590	W1 : $4f(\frac{1}{3}, \frac{2}{3}, 0.1375)$	0.7440
	W2 : $2d(\frac{1}{3}, \frac{2}{3}, \frac{3}{4})$	0.8266	B1 : $4f(\frac{1}{3}, \frac{2}{3}, 0.9766)$	0.9177
	B1 : $12i(0.3333, 0, 0)$	1	B2 : $2d(\frac{1}{3}, \frac{2}{3}, \frac{3}{4})$	1
	B2 : $6h(0.1191, 0.2382, \frac{1}{4})$	0.3735	B3 : $2b(0, 0, \frac{1}{4})$	0.6475
W_{Uiso}, B_{Uiso}	0.0012, 0.0020		0.0007, 0.0028	
VEC (electrons/cell)	9.88		9.69	
wR_P (%), χ^2	2.70, 4.23		5.43, 8.43	

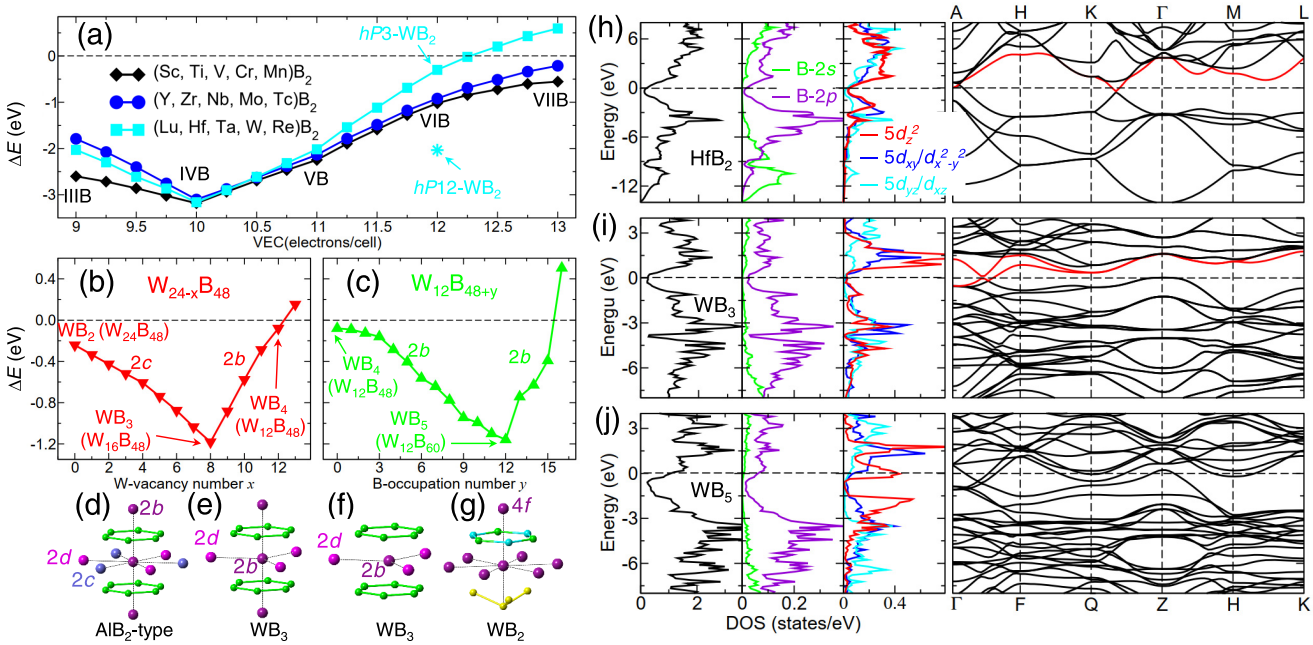

FIG. 5. Calculated formation energies (ΔE), density of states (DOS), and electronic band structures for transition-metal (TM) borides. (a) ΔE vs valence-electron concentration (VEC) for $3d$-, $4d$- and $5d$-TMB_2. Borides with fractional VEC values (e.g., 9.25, 9.5, and 9.75) can be formed by containing both the nearest-neighboring metals in different molar ratios of 3:1, 1:1, and 1:3 [e.g., $(Sc_{0.75}Ti_{0.25})B_2$, $(Sc_{0.5}Ti_{0.5})B_2$, and $(Sc_{0.25}Ti_{0.75})B_2$]. (b) ΔE vs metal vacancy (x) at the Wyckoff $2c(\frac{1}{3}, \frac{2}{3}, \frac{1}{4})$ (i.e., $x = 0$–8) and $2b(0, 0, \frac{1}{4})$ (i.e., $x = 8$–13) for the AlB_2-type $W_{24-x}B_{48}$ supercell [see Fig. 1(a)]. (c) ΔE vs occupation of excess boron (y) at the Wyckoff $6h(x, 2x, \frac{1}{4})$ for the $W_{12}B_{48+y}$ supercell with a metal-deficient AlB_2-type structure (i.e., the $2c$ and $2b$ sites are fully and half unoccupied by W, respectively). All energies are rescaled for one TMB_x formula in a primitive cell. (d)–(g) Structural units for $hP3$-WB_2, WB_3, and $hP12$-WB_2. (h)–(j) Total and partially projected DOS and band structures for HfB_2, WB_3, and WB_5. The Fermi levels at 0 eV are denoted with horizontal dashed lines.

and $2d$ sites possess largely different vacancies, although they come from the same planar B sheet, signaling nonrandom vacancies in the planar B sheet. This occupation disparity between $2b$ and $2d$ sites is likely due to their different local bonding states. Obviously, no boron atom from the adjacent wrinkled B sheets can overlap with B : $2b$ atoms along the c axis, in contrast to that of B : $2d$ atoms. Most intriguingly, both $WB_{5.14}$ and $WB_{2.34}$ have nearly the same valence-electron concentration (VEC) of ∼10 per cell (Table I), indicating a similar electronic mechanism for governing their structural stabilities. Additionally, no phase transition is observed in both borides at low temperatures (Fig. S12 in the Supplemental Material [48]); we also refined their structures and compositions at 7 K (Table S1 in the Supplemental Material [48]) with results like the cases at 300 K.

To explore the underlying formation mechanisms for both borides, we systematically evaluated the formation energy for $hP3$-diborides of $3d$-, $4d$-, and $5d$-TM series to establish the relation of structural stability and VEC (Fig. 5). The calculated energies for these $hP3$-TMB_2 series have a similar trend as the VEC varies [Fig. 5(a)]; a global minimum occurs at an optimal value of 10 per cell for achieving the highest stability (e.g., TiB_2). However, $hP3$-WB_2 possesses a VEC of 12 per cell with a large formation energy, accounting for its instability. By contrast, $hP12$-WB_2 with staggered and wrinkled boron sheets is thermodynamically more favorable with a dramatically reduced formation energy [Fig. 5(a)].

In fact, $WB_{5.14}$ can be viewed as a structural derivative of $hP3$-WB_2 by introducing metal vacancies and boron trimers, as demonstrated in Fig. 1. Thus, we constructed a $hP3$ supercell of $W_{24-x}B_{48+y}$ and calculated its formation energy with varying x and y to evaluate its stability. As expected, the increase of vacancy at W : $2c$ gradually decreases the formation energy of $W_{24-x}B_{48}$ [Fig. 5(b)], achieving a valley value at $x = 8$ that corresponds to the ideal WB_3 model with fully unoccupied $2c$. Before adding an interstitial B3 trimer, we continue taking W out of the structure from the $2b$ site, leading to the increase of formation energy. To accommodate the refined occupancy of W : $2b$ (i.e., ∼0.5; Table I), half W : $2b$ atoms are randomly removed and result in an unstable phase WB_4 at $x = 12$ with a higher energy. Filling the vacant W : $2b$ in WB_4 (i.e., $W_{12}B_{48+y}$) with B atoms as an approximate replacement for boron trimer rapidly lowers its formation energy [Fig. 5(c)]; an energy valley is reached when 12 B are added (i.e., $y = 12$), followed by an increase of energy with adding more B atoms. Obviously, the most stable composition WB_5 (i.e., $W_{12}B_{60}$) occurs at the bottom of the valley, excellently rationalizing our refined $WB_{5.14}$. Additionally, the added 12 B atoms in WB_5 are randomly distributed in four vacant W : $2b$ sites with an average occupation number of 3, equivalent to the filling of a B3 trimer at each site.

To gain insights into their formation mechanisms, we explored electronic properties of the associated borides with key structural units shown in Figs. 5(d)–5(g). By contrast to the AlB_2-type structure [Fig. 5(d)], the absence of W : $2c$ in WB_3 forms honeycomb W layers that are alternately stacked with planar B sheets in two distinct stacking modes (Figs. 5(e), 5(f), S13, and S14 in the Supplemental Material

[48]). A relative shift of the wrinkled B sheet in $hP12$-WB_2 leads to a new bonding sequence of B-W-W along the c axis [Fig. 5(g)]. Using $hP3$-HfB_2 with an optimal VEC of 10 per cell as an illustrative case, we calculated its electronic band structure and density of states (DOS) and plotted them in Fig. 5(h), showing a significant overlap of the states from metal and B with a Fermi level pinned at the bottom of a pseudogap, indicating a strong metal-B bonding. Below the Fermi level, the bonding states contain five degenerated bands and can be grouped into two groups of high- and low-energy bands, which are formed by hybridizations of $5d_{xy}$, $5d_{x^2-y^2}$, and B : $2p_{x/y}$ and of $5d_{yz}$, $5d_{xz}$, and nonbonding B : $2p_z$ states, respectively. Apparently, these five bands are capable of being filled with a maximum VEC of 10 per cell, which explains the reason why $hP3$-diborides have an optimal VEC of 10 per cell [Fig. 5(a)]. Further increase of VEC will cause the filling of $5d_{z^2}$ in the antibonding band above the Fermi level. However, the $5d_{z^2}$ orbital is linked to the direct TM-TM interaction along the c axis, perpendicular to the B layers [Fig. 5(d)], and hence destabilizes the $hP3$ phase. Thus, instability of $hP3$-WB_2 results from fully occupied $5d_{z^2}$ states.

Removing the W : $2c$ atoms from $hP3$-WB_2 creates WB_3 with an optimal VEC of 10 [Fig. 5(i)], satisfying the criterion for forming a stable phase with calculated DOS and band structures resembling those of HfB_2. In WB_3, the $5d_{z^2}$ states of W : $2b$ atoms are completely depleted in Fig. 5(f), while those in Fig. 5(e) should be partially filled due to the existence of strong W-W repulsions along the c axis [4], as also indicated by a slightly occupied $5d_{z^2}$ band across the Fermi level [Fig. 5(i)]. Overfilling of such unfavorable $5d_{z^2}$ states would induce structural instability, hence the occurrence of vacant W : $2b$ to reduce VEC for achieving a stable state. On the other hand, if the bonding bands below the Fermi level are less filled, the system will also become unstable with increased formation energy, as occurred in WB_4 with only half-filled W : $2b$ [Fig. 5(b)]. The insertion of B3 trimers at the vacant W : $2b$ compensates the reduction of VEC for the formation of WB_5; coupling of the trimer and two adjacent B layers produces a key structural unit of a B15 tetradecagon that can sufficiently strengthen its structure and mechanical properties [41]. The calculated DOS and band structure for WB_5 are like those of WB_3 with strongly overlapped and hybridized bonding states between W and B, giving rise to a broad pseudogap around the Fermi level [Fig. 5(j)]. These properties further confirm that WB_5 is an energetically favorable phase.

Staggering the boron sheets of $hP3$-WB_2 provides an alternative approach to relieve the filling of the unfavorable antibonding state of $5d_{z^2}$ by transferring electrons to the $5d_{z^2}$-B : p_z bonding band [Fig. 5(g)], leading to the puckering of staggered B sheets, like that observed in ReB_2 [4]. As a result, $hP12$-WB_2 is formed with a sharp reduction of the formation energy [Fig. 5(a)], although it has a large VEC of 12 per cell. However, our experiments showed that only defective $hP12$-WB_2 can be synthesized with a realistic composition of $WB_{2.34}$. Interestingly, the VEC value of $WB_{2.34}$ is 9.69 close to 10 per cell, suggesting its phase stability should also be dictated by a similar electronic mechanism. Further theoretical work on $WB_{2.34}$ is warranted for exploring its electronic properties and the crucial role of vacancies played in this material by calculations.

IV. CONCLUSIONS

In summary, we have formulated a high-P method for the synthesis of boron-free WB_{3+x} and WB_{2+x} samples. Based on these samples, high-quality neutron diffraction data are collected and refined for solving their longstanding structural ambiguities. The determined compositions for both borides are $WB_{5.14}$ and $WB_{2.34}$ with a similar VEC of $\sim$10 per cell, obeying our established criterion for the formation of stable hexagonal boron-rich borides. Several previously unidentified structural features are also unveiled for both compounds, including the misassigned W : $2c$ site in WB_{3+x} and unique atomic deficiencies in WB_{2+x}. Our findings offer powerful insights into the electronic origin of atomic vacancies in boron-rich borides, which is crucial for understanding their structural stability and formation mechanism. The definitively resolved crystal structures for both borides would provide important foundations for study of their structure-property relationships and for rational design of borides with enhanced properties by tailoring crystalline defects.

The data that support the findings of this study are available from the corresponding authors upon reasonable request.

ACKNOWLEDGMENTS

This paper was supported by the Key Research Platforms and Research Projects of Universities in Guangdong Province (Grant No. 2018KZDXM062), the Guangdong Innovative & Entrepreneurial Research Team Program (Grant No. 2016ZT06C279), the Shenzhen Peacock Plan (Grant No. KQTD2016053019134356), the Shenzhen Development and Reform Commission Foundation for Shenzhen Engineering Research Center for Frontier Materials Synthesis at High Pressure, the Shenzhen Science and Technology Innovation Committee (Grant No. JCYJ20190809173213150), and the Research Platform for Crystal Growth &Thin-Film Preparation at SUSTech. We also acknowledge the support of the National Natural Science Foundation of China (Grants No. 52032001 and No. 51671126) and the Shanghai Natural Science Foundation (Grant No. 20ZR1400900). A portion of this research used resources at the Spallation Neutron Source, a DOE Office of Science User Facility operated by Oak Ridge National Laboratory, USA.

The authors declare no competing interests.

[1] H. Hubert, B. Devouard, L. A. J. Garvie, M. O'Keeffe, P. R. Buseck, W. T. Petuskey, and P. F. McMillan, Icosahedral packing of B12 icosahedra in boron suboxide (B_6O), Nature **391**, 376 (1998).

[2] A. R. Oganov, J. Chen, C. Gatti, Y. Ma, Y. Ma, C. W. Glass, Z. Liu, T. Yu, O. O. Kurakevych, and V. L. Solozhenko, Ionic high-pressure form of elemental boron, Nature **457**, 863 (2009).

[3] Z. Zhang, E. S. Penev, and B. I. Yakobson, Polyphony in B flat, Nat. Chem. **8**, 525 (2016).

[4] J. K. Burdett, E. Canadell, and G. J. Miller, Electronic structure of transition-metal borides with the AlB_2 structure, J. Am. Chem. Soc. **108**, 6561 (1986).

[5] R. Mohammadi, A. T. Lech, M. Xie, B. E. Weaver, M. T. Yeung, S. H. Tolbert, and R. B. Kaner, Tungsten tetraboride, an inexpensive superhard material, Proc. Natl. Acad. Sci. USA **108**, 10958 (2011).

[6] J. B. Levine, S. H. Tolbert, and R. B. Kaner, Advancements in the search for superhard ultra-incompressible metal borides, Adv. Funct. Mater. **19**, 3519 (2009).

[7] J. V. Rau, A. Latini, R. Teghil, A. De Bonis, M. Fosca, R. Caminiti, and V. Rossi Albertini, Superhard tungsten tetraboride films prepared by pulsed laser deposition method, ACS Appl. Mater. Inter. **3**, 3738 (2011).

[8] C. Liu, F. Peng, N. Tan, J. Liu, F. Li, J. Qin, J. Wang, Q. Wang, and D. He, Low-compressibility of tungsten tetraboride: a high pressure x-ray diffraction study, High Pressure Res. **31**, 275 (2011).

[9] M. Xie, R. Mohammadi, Z. Mao, M. M. Armentrout, A. Kavner, R. B. Kaner, and S. H. Tolbert, Exploring the high-pressure behavior of superhard tungsten tetraboride, Phys. Rev. B **85**, 064118 (2012).

[10] R. Mohammadi, M. Xie, A. T. Lech, C. L. Turner, A. Kavner, S. H. Tolbert, and R. B. Kaner, Toward inexpensive superhard materials: tungsten tetraboride-based solid solutions, J. Am. Chem. Soc. **134**, 20660 (2012).

[11] L. Xiong, J. Liu, L. Bai, Y. Li, C. Lin, D. He, F. Peng, and J.-F. Lin, Radial x-ray diffraction of tungsten tetraboride to 86 GPa under nonhydrostatic compression, J. Appl. Phys. **113**, 033507 (2013).

[12] M. Wang, Y. Li, T. Cui, Y. Ma, and G. Zou, Origin of hardness in WB_4 and its implications for ReB_4, $Ta B_4$, MoB_4, TcB_4, and OsB_4, Appl. Phys. Lett. **93**, 101905 (2008).

[13] X. Cheng, X.-Q. Chen, D. Li, and Y. Li, Computational materials discovery: the case of the W-B system, Acta Crystallogr. C **70**, 85 (2014).

[14] Q. Tao, D. Zheng, X. Zhao, Y. Chen, Q. Li, Q. Li, C. Wang, T. Cui, Y. Ma, X. Wang, and P. Zhu, Exploring hardness and the distorted sp^2 hybridization of B-B bonds in WB_3, Chem. Mater. **26**, 5297 (2014).

[15] Y. Liang, J. Yang, X. Yuan, W. Qiu, Z. Zhong, J. Yang, and W. Zhang, Polytypism in superhard transition-metal triborides, Sci. Rep. **4**, 5063 (2014).

[16] Y. Liang, Z. Wu, X. Yuan, W. Zhang, and P. Zhang, Discovery of elusive structures of multifunctional transition-metal borides, Nanoscale **8**, 1055 (2016).

[17] Q. Li, D. Zhou, W. Zheng, Y. Ma, and C. Chen, Anomalous Stress Response of Ultrahard WB_n Compounds, Phys. Rev. Lett. **115**, 185502 (2015).

[18] H. Wu, H. Sun, and C. Chen, Unexpected structural softening of interstitial boron solid solution WB_{3+x}, Appl. Phys. Lett. **105**, 211901 (2014).

[19] Q. Gu, G. Krauss, and W. Steurer, Transition metal borides: superhard versus ultra-incompressible, Adv. Mater. **20**, 3620 (2008).

[20] R. Kiessling, A. Wetterholm, L. G. Sillén, A. Linnasalmi, and P. Laukkanen, The crystal structures of molybdenum and tungsten borides, Acta Chem. Scand. **1**, 893 (1947).

[21] P. A. Romans and M. P. Krug, Composition and crystallographic data for the highest boride of tungsten, Acta Crystallogr. **20**, 313 (1966).

[22] H. Duschanek and P. Rogl, Critical assessment and thermodynamic calculation of the binary system boron-tungsten (B-W), J. Phase Equilib. **16**, 150 (1995).

[23] I. Zeiringer, P. Rogl, A. Grytsiv, J. Polt, E. Bauer, and G. Giester, Crystal structure of $W_{1-x}B_3$ and phase equilibria in the boron-rich part of the systems Mo-Rh-B and W-{Ru,Os,Rh,Ir,Ni,Pd,Pt}-B, J. Phase Equilib. Diffus. **35**, 384 (2014).

[24] E. Zhao, J. Meng, Y. Ma, and Z. Wu, Phase stability and mechanical properties of tungsten borides from first principles calculations, Phys. Chem. Chem. Phys. **12**, 13158 (2010).

[25] Y. Liang, X. Yuan, and W. Zhang, Thermodynamic identification of tungsten borides, Phys. Rev. B **83**, 220102(R) (2011).

[26] R. F. Zhang, D. Legut, Z. J. Lin, Y. S. Zhao, H. K. Mao, and S. Veprek, Stability and Strength of Transition-Metal Tetraborides and Triborides, Phys. Rev. Lett. **108**, 255502 (2012).

[27] Y. Liang, Y. Gou, X. Yuan, Z. Zhong, and W. Zhang, Unexpectedly hard and highly stable WB_3 with a noncompact structure, Chem. Phys. Lett. **580**, 48 (2013).

[28] Q. Li, D. Zhou, W. Zheng, Y. Ma, and C. Chen, Global Structural Optimization of Tungsten Borides, Phys. Rev. Lett. **110**, 136403 (2013).

[29] H. Gou, Z. Li, L.-M. Wang, J. Lian, and Y. Wang, Peculiar structure and tensile strength of WB_4: nonstoichiometric origin, AIP Adv. **2**, 012171 (2012).

[30] Y. Liang, Z. Fu, X. Yuan, S. Wang, Z. Zhong, and W. Zhang, An unexpected softening from WB_3 to WB_4, EPL-Europhys. Lett. **98**, 66004 (2012).

[31] C. Zang, H. Sun, and C. Chen, Unexpectedly low indentation strength of WB_3 and MoB_3 from first principles, Phys. Rev. B **86**, 180101(R) (2012).

[32] H. Nowotny, H. Haschke, and F. Benesovsky, Bor-reiche wolframboride, Monatsh. Chem. **98**, 547 (1967).

[33] X. Cheng, W. Zhang, X.-Q. Chen, H. Niu, P. Liu, K. Du, G. Liu, D. Li, H.-M. Cheng, H. Ye, and Y. Li, Interstitial-boron solution strengthened WB_{3+x}, Appl. Phys. Lett. **103**, 171903 (2013).

[34] T. Lundström and I. Rosenberg, The crystal structure of the molybdenum boride $Mo_{1-x}B_3$, J. Solid State Chem. **6**, 299 (1973).

[35] A. T. Lech, C. L. Turner, R. Mohammadi, S. H. Tolbert, and R. B. Kaner, Structure of superhard tungsten tetraboride: a missing link between MB_2 and MB_{12} higher borides, Proc. Natl. Acad. Sci. USA **112**, 3223 (2015).

[36] H. P. Woods, F. E. Wawner, Jr., and B. G. Fox, Tungsten diboride: preparation and structure, Science **151**, 75 (1966).

[37] T. Lundström, The structure of Ru_2B_3 and $WB_{2.0}$ as determined by single-crystal diffractometry, and some notes on the W-B system, Arkiv Kemi **30**, 115 (1969).

[38] S. Otani, H. Ohashi, and Y. Ishizawa, Lattice constants and nonstoichiometry of WB_{2-x}, J. Alloys Compd. **221**, L8 (1995).

[39] X.-Q. Chen, C. L. Fu, M. Krčmar, and G. S. Painter, Electronic and Structural Origin of Ultraincompressibility of 5*d*

Transition-Metal Diborides MB_2 (M = W, Re, Os), Phys. Rev. Lett. **100**, 196403 (2008).

[40] V. F. Sears, Neutron scattering lengths and cross sections, Neutron News **3**, 26 (1992).

[41] W. Gong, C. Liu, X. Song, Q. Li, Y. Ma, and C. Chen, Unravelling the structure and strength of the highest boride of tungsten $WB_{4.2}$, Phys. Rev. B **100**, 220102(R) (2019).

[42] A. Kvashnin, D. Rybkovskiy, V. Filonenko, V. Bugakov, I. Zibrov, V. Brazhkin, A. Oganov, A. Osiptsov, and A. Zakirov, WB_{5-x}: synthesis, properties, and crystal structure—new insights into the long-debated compound, Adv. Sci. **7**, 2000775 (2020).

[43] J. Dong, H. Li, J. Wang, Z. Guo, J. Liao, X. Hao, X. Zhang, and D. Chen, Nonrandomly distributed tungsten vacancies and interstitial boron trimers in tungsten tetraboride, J. Phys. Chem. C **123**, 29314 (2019).

[44] A. G. Kvashnin, H. A. Zakaryan, C. M. Zhao, Y. F. Duan, Y. A. Kvashnina, C. W. Xie, H. F. Dong, and A. R. Oganov, New tungsten borides, their stability and outstanding mechanical properties, J. Phys. Chem. Lett. **9**, 3470 (2018).

[45] C. Zhao, Y. Duan, J. Gao, W. Liu, H. Dong, H. Dong, D. Zhang, and A. R. Oganov, Unexpected stable phases of tungsten borides, Phys. Chem. Chem. Phys. **20**, 24665 (2018).

[46] X. Zhou, D. Ma, L. Wang, Y. Zhao, and S. Wang, Large-volume cubic press produces high temperatures above 4000 Kelvin for study of the refractory materials at pressures, Rev. Sci. Instrum. **91**, 015118 (2020).

[47] B. H. Toby, EXPGUI, a graphical user interface for GSAS, J. Appl. Cryst. **34**, 210 (2001).

[48] See Supplemental Material at http://link.aps.org/supplemental/10.1103/PhysRevB.104.014110 for experimental details of NPD, XRD, and SEM measurements and crystal structures analysis for WB_{3+x} and WB_{2+x} samples.

[49] G. Kresse and J. Furthmüller, Efficient iterative schemes for *ab initio* total-energy calculations using a plane-wave basis set, Phys. Rev. B **54**, 11169 (1996).

[50] P. E. Blöchl, Projector augmented-wave method, Phys. Rev. B **50**, 17953 (1994).

[51] J. P. Perdew, K. Burke, and M. Ernzerhof, Generalized Gradient Approximation Made Simple, Phys. Rev. Lett. **77**, 3865 (1996).

[52] H. Tang *et al.*, Boron-rich molybdenum boride with unusual short-range vacancy ordering, anisotropic hardness, and superconductivity, Chem. Mater. **32**, 459 (2020).

[53] A. Chretien and J. Helgorsky, Sur les borures de molybdene et de tungstene MoB_4 et WB_4 composes nouveaux, C.R. Acad. Sci. **252**, 742 (1961).

[54] D. Portehault, S. Devi, P. Beaunier, C. Gervais, C. Giordano, C. Sanchez, and M. Antonietti, A general solution route toward metal boride nanocrystals, Angew. Chem. Int. Edit. **50**, 3262 (2011).

[55] L. Chen, Y. Gu, Y. Qian, L. Shi, Z. Yang, and J. Ma, A facile one-step route to nanocrystalline TiB_2 powders, Mater. Res. Bull. **39**, 609 (2004).

[56] L. Zoli, P. Galizia, L. Silvestroni, and D. Sciti, Synthesis of group IV and V metal diboride nanocrystals via borothermal reduction with sodium borohydride, J. Am. Ceram. Soc. **101**, 2627 (2018).

[57] S. Wang, H. Ge, S. Sun, J. Zhang, F. Liu, X. Wen, X. Yu, L. Wang, Y. Zhang, H. Xu, J. C. Neuefeind, Z. Qin, C. Chen, C. Jin, Y. Li, D. He, and Y. Zhao, A new molybdenum nitride catalyst with rhombohedral MoS_2 structure for hydrogenation applications, J. Am. Chem. Soc. **137**, 4815 (2015).

[58] S. Wang, J. Zhang, D. He, Y. Zhang, L. Wang, H. Xu, X. Wen, H. Ge, and Y. Zhao, Sulfur-catalyzed phase transition in MoS_2 under high pressure and temperature, J. Phys. Chem. Solids **75**, 100 (2014).

[59] K. S. Liang, R. R. Chianelli, F. Z. Chien, and S. C. Moss, Structure of poorly crystalline MoS_2—a modeling study, J. Non-Cryst. Solids **79**, 251 (1986).

[60] O. Kafri and I. Glatt, The physics of moiré metrology, Precis. Eng. **13**, 77 (1991).

[61] X. Hao, Y. Xu, Z. Wu, D. Zhou, X. Liu, X. Cao, and J. Meng, Low-compressibility and hard materials ReB_2 and WB_2: prediction from first-principles study, Phys. Rev. B **74**, 224112 (2006).